THE UNIVERSITY OF SYDNEY

SCHOOL OF CIVIL ENGINEERING

STRENGTHS AND FRACTURE STRAINS OF WELD AND HAZ IN WELDED CONNECTIONS

RESEARCH REPORT R973

X LIU
S YAN
K J R RASMUSSEN
G G DEIERLEIN

February 2023

ISSN 1833-2781

Copyright Notice

School of Civil Engineering, Research Report R972
Strengths and fracture strains of weld and HAZ in welded connections
X Liu MScEng
S Yan PhD
K J R Rasmussen MScEng PhD Deng
G G Deierlein MScEng PhD
February 2023

ISSN 1833-2781

Published by:
School of Civil Engineering
The University of Sydney
Sydney NSW 2006
Australia

Abstract

This paper investigates the strengths and fracture strains of weld and heat affected zone (HAZ) in welded connections for both the longitudinal and transverse directions and compares them to those of the base metal. A series of miniature coupons, including miniature flat plates, notched round bars and grooved plates, were extracted from the three zones of a butt weld and tested using a custom-built jig. The true stress-strain relationships and fracture strains of the base metal, weld and HAZ materials were obtained for both directions from the miniature coupon tests and corresponding numerical simulations. The fracture strain data were used to calibrate the Lode angle modified void growth model (LMVGM) for predicting the fracture strain of the three material zones at any given stress state. The following major conclusions were drawn: (1) The weld was generally isotropic in terms of both strength and fracture strain. The weld also had the highest values of yield and tensile strengths among the three materials in both directions, but the lowest fracture strain in both directions except for the longitudinal direction with stress triaxiality above 0.21 to 0.30, for which the base metal had the lowest fracture strain. (2) The HAZ had higher yield and tensile strengths but smaller fracture strain in the longitudinal direction than in the transverse direction. The same anisotropic characteristic applied to the base metal. Meanwhile, the HAZ had higher yield and tensile strengths than the base metal as well as similar but slightly larger fracture strains in both directions. (3) The yield and tensile strengths of the weld and HAZ can be approximated using the empirical hardness-strength correlation functions, except that the functions tend to overestimate the strengths of the weld by about 10%. (4) For the weld, HAZ and base metal, the fracture surfaces tilted towards stress states with high stress triaxiality and low Lode angle parameter, indicating that fracture can initiate more easily at these stress states. Note that the above conclusions are limited to the tested AS350 grade steel and the selected welding parameters.

Keywords: Welded connections, heat affected zone, miniature coupons, stress-strain curves, fracture

Table of Content

1 INTRODUCTION

Welded connections are widely used in steel structures to connect structural members. The weld zone of a fusion weld always includes, from the centreline of the weld outward, a fusion zone, a heat-affected zone (HAZ), and an unaffected base metal zone (BM). Materials in the three zones have different chemical compositions (i.e., fusion material vs. base metal) or different microstructures (i.e., HAZ vs. base metal), and correspondingly have different mechanical properties [1, 2]. In the analysis or finite-element (FE) simulations of welded connections, however, the materials in the fusion zone and HAZ are normally assigned the same properties as the base metal [3, 4], partly for the sake of simplicity and partly due to the lack of experimental data for the properties of the fusion and HAZ materials. However, this simplified assumption may lead to an inaccurate prediction of the ultimate resistance of connections because experiments on welded connections have demonstrated that fracture often initiates in the fusion zone or HAZ [5, 6]. Therefore, it is imperative to distinguish the material properties, in particular the strength and fracture strain, of the fusion and HAZ materials from those of the base metal.

The strengths and stress-strain curves of metals can be easily obtained through standard tensile coupon tests. However, in cross-section, the scale of conventional coupons is of the order of a centimetre, which is larger than the width of a HAZ, normally between 2 to 5 mm [7]. Hence, four alternative methods have been used to obtain the properties of the weld and HAZ materials: 1) Perform the Vickers hardness test and then compute the material yield stress and tensile strength through empirical hardness-strength correlation functions [8-10]. This method is relatively simple, but its accuracy highly depends on the precision of the correlation functions, which are material dependent. 2) Perform tests on miniature coupons, the cross-sectional dimension of which is no larger than a few millimetres, extracted from the weld or HAZ [11, 12]. The stress-strain response of the weld and HAZ materials can thus be directly obtained, but the tests require special setup and care to guarantee accurate test results. 3) Use the Gleeble Welding Simulator to reproduce the same thermal cycle on the base metal as that the HAZ is experiencing, thus producing HAZ material in a large volume, from which conventional size coupons can be extracted and tested [13, 14]. However, Gleeble Welding Simulators are not accessible. 4) Use Digital Image Correlation (DIC) to measure strains in the fusion zone and HAZ. The material properties can then be obtained based on certain assumptions about the stress distribution in the welded area [15, 16]. However, since DIC measures the surface strain only, this method is less accurate for bulk material.

A large number of coupon tests have been conducted to evaluate fracture strains of base metal materials. It is well known that the fracture strain of a ductile metal is notably affected by the stress state, and so coupons have been designed with various geometries to generate different stress states [17-21], e.g., notched round bars for axisymmetric tri-axial tension states and grooved plates for plane strain tri-axial tension states. However, seeing that the dimensions of standard coupons are

larger than the weld and HAZ [20, 21], miniature coupons have been extracted from these area to determine fracture strains. Mae et al. [22] tested mini-notched and unnotched bars and mini-flat butterfly coupons to characterise the fracture properties of a cast aluminium alloy. Gorji et al. [23] conducted experiments on aluminium alloy 6016-T4 using miniature uniaxial tension coupons, notched tension coupons, central hole coupons and smiley shear coupons. Pandya et al. [24] developed a micro-tensile testing technique to characterise the fracture strains of the weld and HAZ materials in a resistance spot weld of dual-phase steel sheets.

Despite the many tests summarised above, limited experimental data is available for structural steel weld and HAZ materials, and the differences in material properties (fracture strain, in particular) in the longitudinal and transverse directions are rarely discussed. In light of this, this paper aims to measure and compare the strengths and fracture strains of the weld, HAZ and base materials in both the longitudinal and transverse directions. Considering that testing miniature coupons is the only reliable method to measure the material properties of the weld and HAZ, a series of miniature coupons, including miniature flat plates, notched round bars and grooved plates, were designed and extracted from the three zones of a butt weld connecting two AS350 grade steel plates [25]. The tests were performed using a novel test jig specially designed for the miniature coupons. Macroetching and hardness tests were also performed; the former to identify the three zones, while the latter was used to compare the hardness of the three material areas. Based on the results of the miniature coupon tests and fully nonlinear FE simulations thereof, the true stress-strain relationships and fracture strains of the base metal, weld and HAZ materials were obtained for both directions. The fracture strain data were then used to calibrate the Lode angle modified void growth model (LMVGM), predicting the fracture loci over the full range of stress states. The differences between the properties of the base metal, weld and HAZ materials are highlighted for both the longitudinal and transverse directions.

2 EXPERIMENTAL PROGRAM

2.1 MATERIALS AND WELDING

A butt weld with a single V-groove preparation prequalified to [26] was used to connect two AS350 grade steel plates [25] with the same nominal thickness of 10 mm,. The longitudinal, transverse and normal directions are defined in Fig.1, where the longitudinal direction was the same as the rolling direction of the steel plate. The weld was laid using Gas Metal-Arc Welding (GMAW), the welding wire was of grade B-G49 [26], and the shielding gas was 18% CO_2 bal Ar. The welding voltage ranged from 23 V to 26 V, the current ranged from 200 A to 220 A, and the welding speed ranged from 200 mm/min to 250 mm/min. Weld Australia was consulted to review the Welding Procedure Specifications (WPSes) and confirmed the WPSes satisfied the requirements of AS 1554.1 SP Category [26]. A Weld Australia representative was present during the welding to help ensure the specified welding parameters were correctly used for the welds.

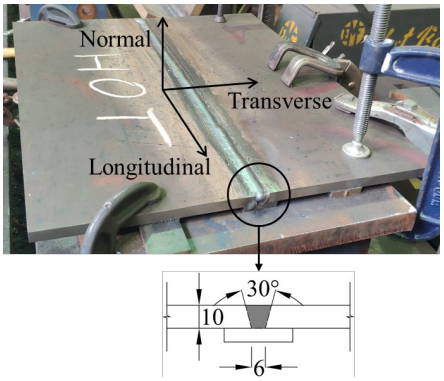

Fig. 1. Single V-groove butt weld

2.2 MACROETCHING AND HARDNESS TESTS

To identify the fusion zone and HAZ, the butt welded specimen was cut into 16 pieces across the weld, each containing all three zones. The pieces were then mounted in epoxy resin, with the surface ground, polished, and etched using 4% nitric acid. After macro-etching, as shown in Fig. 2(a), the three zones could be distinguished, shown with different colours in Fig. 2(b). The width of the HAZ could then be measured as the distance between the lines dividing the zones. The distance could be measured in different directions, leading to different widths. In this study, both the horizontal distance in the plane of the plate and the nominal net distance in the direction perpendicular to the V-groove (i.e., the direction with a 15° slope) were measured, representing the horizontal width and net width of the HAZ, respectively. For each macro-etched piece, both widths were measured at six different distances from the top surface, providing a total of 96 measurements for both the horizontal and net widths, as shown in Fig. 3. The majority of the measurements ranged between 1.5 mm and 3.0 mm, with the average values of 2.23 mm and 2.08 mm for the horizontal width and net width, respectively. It was also observed that the horizontal width measurements were slightly more variable than the net width measurements.

The Vickers hardness was measured at 18 locations on each macro-etched piece, six in each of the fusion zone, HAZ and base metal zone. The six locations in each zone were randomly selected, sufficiently spaced that the impact areas did not interact. Under the load of 4.9 N (0.5 kg), the average indentation sizes were 77.15 μm, 71.29 μm and 67.32 μm, and the average HV0.5 values were computed as 155.5, 182.7 and 205.3, for the base metal, HAZ and weld, respectively. The weld was the hardest, while the base metal was the softest.

(a) After macro-etching (b) Highlighted with different colours

Fig. 2. Photos of etched surface.

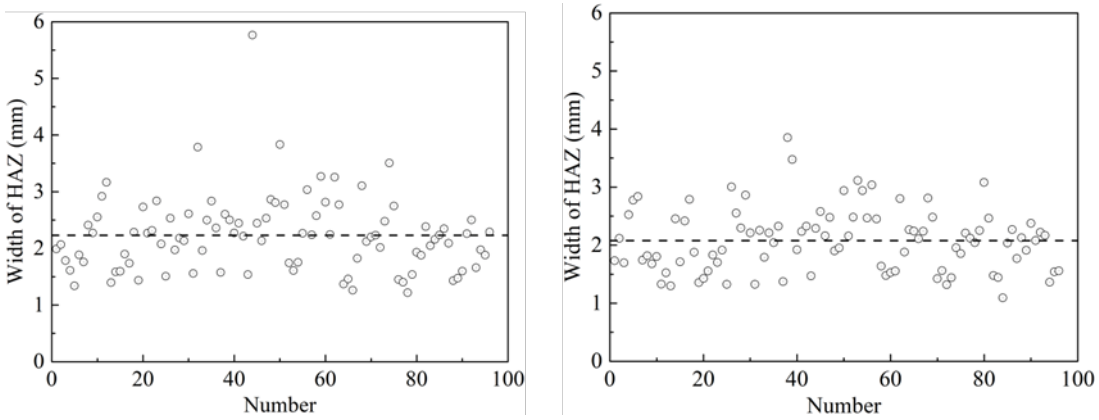

(a) Horizontal width (b) Net width

Fig. 3. Width of HAZ.

2.3 TENSILE COUPON TESTS

2.3.1 Miniature coupons

Miniature flat plate (FP) coupons were tested to obtain the stress-strain response of the materials and the fracture strains corresponding to the uniaxial tension stress state. Another two types of miniature coupons, i.e., the notched round bars (NRB) and grooved plates (GP), were tested to obtain the fracture strains associated with the axisymmetric tri-axial tension states and plane strain tri-axial tension states, respectively. Fig. 4 shows the coupon geometries. It is noted that the specimens were miniature, with the dimensions of the cross-section of interest in the range of 1 mm to 2.5 mm.

The miniature coupons were extracted from all three zones, which were identified according to the macroetching results. Also, the miniature coupons were extracted along both the longitudinal and transverse directions. Fig. 5 exemplifies the locations and directions of extraction for the FP coupons, where the letters "BM" refer to the base metal, "FP" to the flat plate, and "L" and "T" to the longitudinal and transverse directions, respectively.

The longitudinal flat plate coupons (i.e., FPLs), as shown in Fig. 4(a), were proportionally scaled down from standard coupons designed according to [27] (i.e., Fig. 4(e)), having the so-called proportional geometries for which the gauge length is equal to $L_0 = 5.65\sqrt{A_0}$. Hence, with the cross-

section of 2.5 mm × 1 mm, the FPLs had a gauge length of 9.0 mm and a parallel length of 11.4 mm. As the transverse coupons (FPTs) intersected the narrow fusion zone and HAZ, in order to ensure the coupon contained only a single material within its gauge length, the FPTs were designed with the parallel part being only 3 mm long, as shown in Fig. 4(b). Standard coupons shown in Fig. 4(e) were also extracted from the base metal in the longitudinal direction, i.e., FPL-standard, to check agreement between results obtained from standard and miniature coupons cut from the same material.

Figs. 4(c) and 4(d) show the nominal dimensions of the miniature NRB and GP coupons, respectively. The actual dimensions were measured using callipers or, when the measured part was too small for callipers to be used, digital image processing. Six replicated measurements were taken on each FP coupon, three were taken on NRB and GP coupons, and two were taken on FPL-standard coupons. Table 1 summarises the key dimensions, including the diameter and width of the smallest cross-sections of the NRB and GP coupons, respectively.

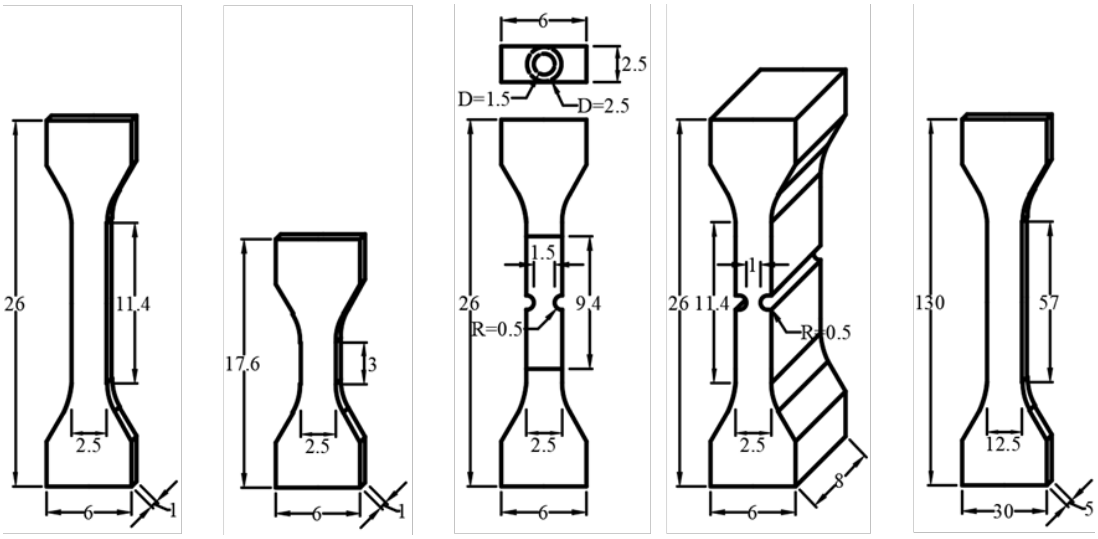

(a) FPL (b) FPT (c) NRB (d) GP (e) FPL-standard

Fig. 4. Geometries and nominal dimensions of coupons (mm).

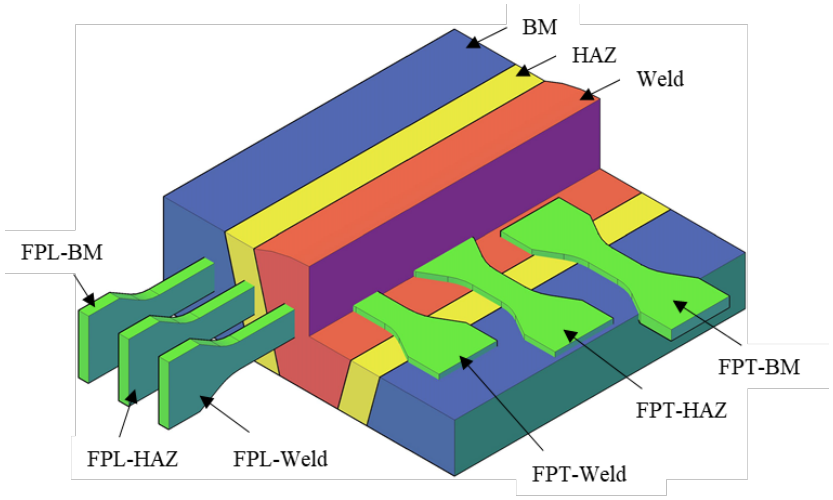

Fig. 5. Location and direction of flat plat (FP) coupons extracted from the butt-welded plates.

Table 1. Measured dimensions of the smallest cross-sections of the NRB and GP coupons (mm).

	NRB – diameter				GP - width			
	1	2	3	Avg.	1	2	3	Avg.
BL	1.51	1.56	1.5	1.52	1.16	1.27	1.18	1.2
WL	1.53	1.55	1.54	1.54	1.18	1.1	1.15	1.14
HL	1.51	1.54	1.53	1.52	1.16	1.13	1.24	1.17
BT	1.55	1.59	1.56	1.56	1.1	1.03	1.25	1.12
WT	1.55	1.53	1.48	1.52	1.2	1.2	1.19	1.19
HT	1.52	1.51	1.56	1.53	1.07	1.05	0.97	1.03

2.3.2 Test jig and measurement

The uniaxial tensile tests were carried out in a 300 kN MTS Sintech testing machine. For the miniature tests, the test frame was equipped with a load cell and a custom-built jig, as shown in Fig. 6.

Due to the small size of the miniature coupons, when performing tension tests, small misalignments may create large bending strains, and gripping can alter or destroy the sample. Hence, the jig for supporting the specimens was customised in this study, consistent in geometry with the specimen dimensions, as shown in Fig. 7. The jig included two grips, each with an open slot in the shape of the ends of the specimen, the transition curves and part of the parallel length, for easy fixing of the miniature coupon and ensuring alignment of the specimen in the grips. A pair of interchangeable spacers were used to accommodate miniature specimens with different thicknesses, held in place by a bolted top cover from each side of the grip. At the end of each grip, a universal joint was used to connect the grip to the support and crosshead of the testing machine. Thus, the axiality of the specimen in the grips was ensured with no bending moment applied to the specimen due to possible misalignments. Two guides were used to facilitate the installation of the specimen into the grips, as well as the installation of the grips in the testing machine. The guides were removed before the commencement of the test to avoid possible friction effects.

The relative displacement between the upper and lower grips was measured independently using a 25 mm extensometer and a DIC system. The measurements using the extensometer and DIC system agreed well with each other, which proved the reliability of the DIC system for determining displacements of the grips and, by implication, the test specimen. The space between the two grips could not accommodate any ordinary extensometer, and therefore, the deformations of the miniature coupons were measured using the DIC system. The gauge length (i.e., L_0) of the DIC measurement was set as 9 mm for all miniature coupons except the miniature FPTs, the gauge length of which was set as 2 mm. It is noted that L_0 = 9.0 mm indicated proportional geometries for the FPLs. The deformations of the standard coupons were measured using an extensometer located in the middle of the parallel length over a gauge length of 25 mm.

To obtain the static load-deformation curves, the loading was controlled at a low speed of 0.1-0.5 mm/min, depending on the deformability of the coupon, and paused two or three times for 100s to allow stress relaxation. The static load-deformation curves were then obtained following the method adopted in [28].

The engineering stress-strain curves of the miniature FPLs and FPL-standard coupons are shown in Fig. 8, where letters "M" and "S" refer to miniature and standard, respectively. The miniature and standard specimens produced very similar curves prior to reaching the ultimate tensile strength, which corresponded to the commencement of necking. In the post-necking range, the engineering strains of the standard specimens are slightly larger than those of the miniature specimens because the deformations of the standard specimens were measured over the 25 mm gauge length, which was shorter than the proportional gauge length (i.e., $L_0 = 5.65\sqrt{A_0} = 44.7$ mm). If the gauge length was taken as 44.7 mm, the engineering stress-strain curves obtained from the miniature and standard coupons would agree well with each other over the full loading range, as proven through FE simulation in Section 3.2 (see Fig. 14). Hence, the accuracy of the miniature testing scheme and the test jig was verified.

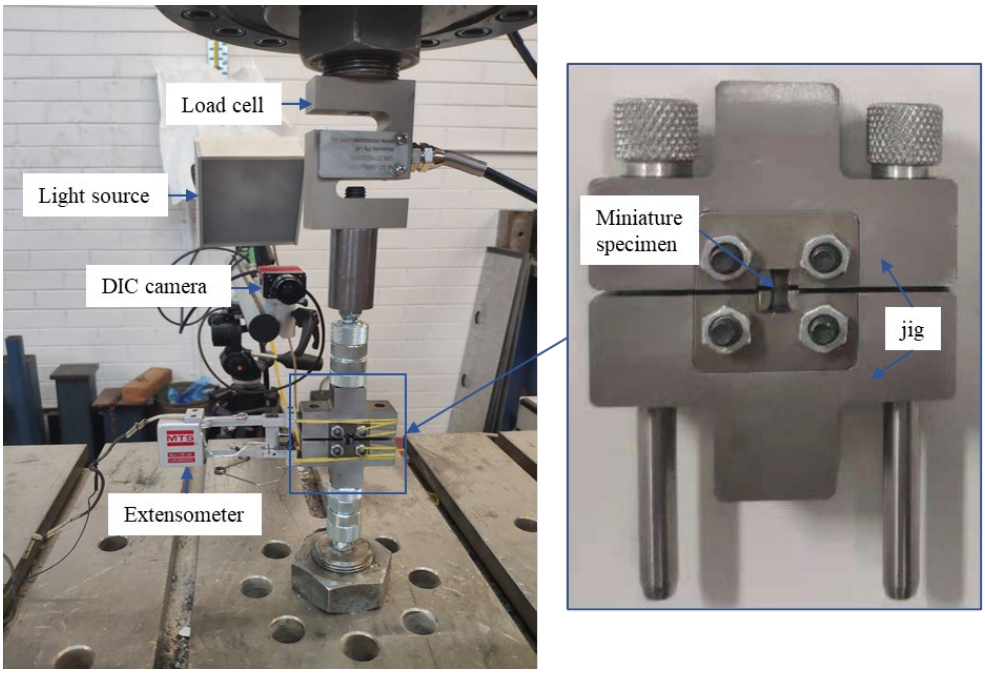

Fig. 6. Test setup of miniature coupons.

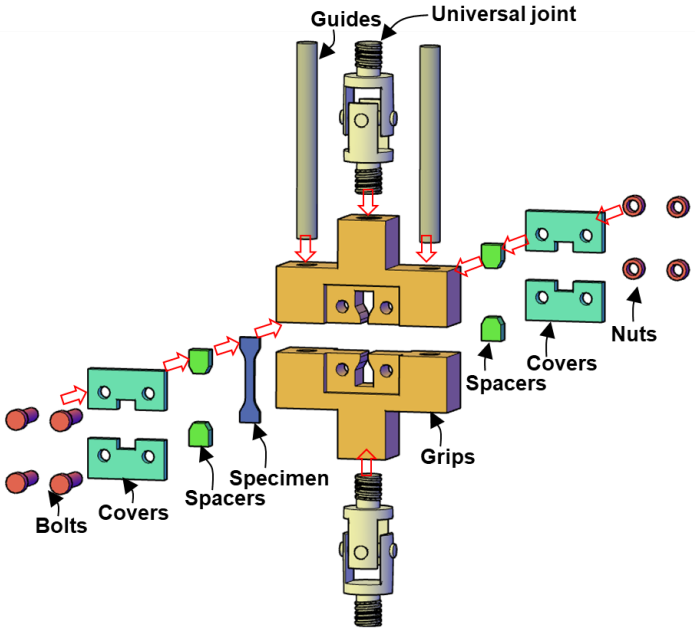

Fig. 7. Design of custom-built miniature testing jig.

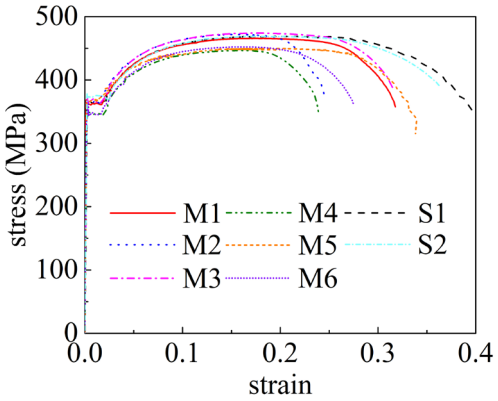

Fig. 8. Engineering stress-strain curves for base metal in the longitudinal direction.

3 FULL-RANGE STRESS-STRAIN RELATIONSHIPS

3.1 TEST RESULTS OF FLAT PLATES

During the loading process of the miniature flat plates, the plastic deformation was highly localised at the parallel part of the coupon where fracture finally occurred, as shown in Fig. 9. The load-deformation curves of the FPLs and FPTs are presented in Figs. 10 and 11. All test curves reached a maximum load when necking commenced and were truncated at the fracture initiation point where a steep drop occurred.

The engineering yield stresses, σ_y, and tensile strength, σ_u, were calculated from each test. The percentage elongation corresponding to the fracture initiation, $\delta_f = D_f / L_0$ was also calculated, where D_f, is the deformation under which fracture occurred. Note that the δ_f values were not comparable between the FPLs and FPTs as they adopted different L_0. The values of σ_y, σ_u, D_f and δ_f are summarised in Tables 2 and 3 for the three materials. The following observations were made:

(1) For both the longitudinal and transverse directions, the curves of the base metal were nearly identical, while those of the weld and HAZ showed large variations in terms of both the onset of yielding and post-yielding response. The large scatter indicated that the stress-strain relationships of the weld and HAZ were less homogeneous than those of the base metal, resulting from the steep temperature gradients near the fusion line.

(2) In both directions, the yield stress and tensile strength of the HAZ were higher than those of the base metal but lower than those of the weld, which was consistent with the hardness test results.

(3) For base metal and HAZ, the yield stress and tensile strength in the longitudinal direction were higher than their transverse counterparts, while the strength of the weld was observed to be nearly independent of the direction.

(4) Based on the comparison of the fracture deformations (and similarly that of the percentage elongations), the base metal showed the largest fracture deformation in both directions, while the HAZ materials showed the smallest.

(a) FPL (b) FPT

Fig. 9. Fractured miniature flat plates for base metal.

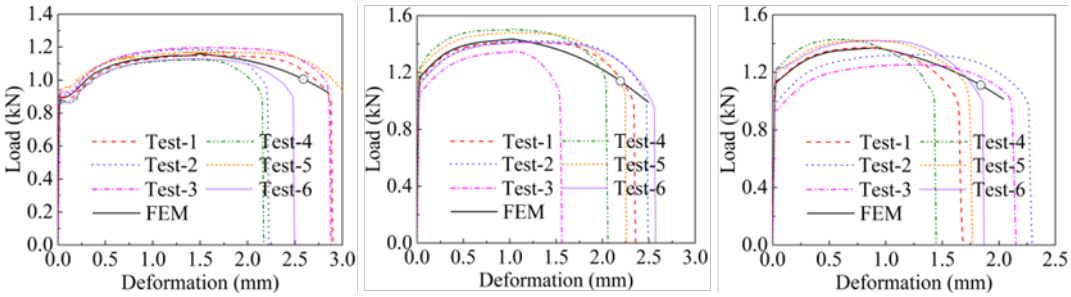

(a) Base metal (b) Weld (c) HAZ

Fig. 10. Load-deformation curves of FPLs.

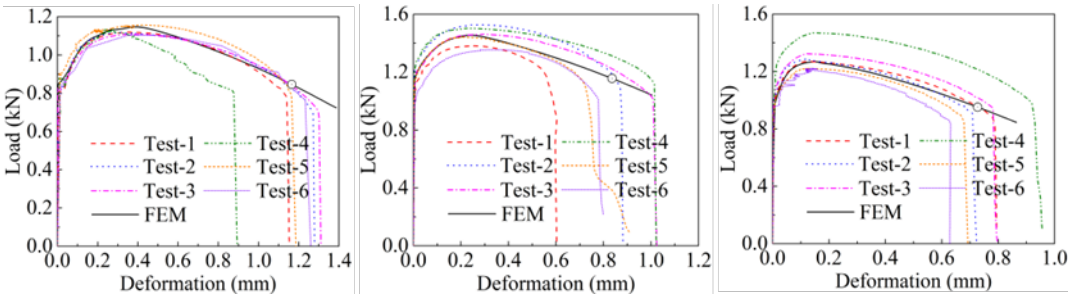

(a) Base metal (b) Weld (c) HAZ

Fig. 11. Load-deformation curves of FPTs.

Table 2. Yield stresses and ultimate tensile strengths (unit: MPa).

	Base metal				Weld				HAZ			
	Longitudinal		Transverse		Longitudinal		Transverse		Longitudinal		Transverse	
	σ_y	σ_u	σ_y	σ_u	σ_y	σ_u	σ_y	σ_u	σ_y	σ_u	σ_y	σ_u
Test-1	360	466	331	458	461	567	444	554	456	549	352	509
Test-2	361	472	328	447	456	570	499	611	395	529	392	515
Test-3	362	474	322	440	424	540	472	585	378	502	383	530
Test-4	350	467	349	456	500	603	465	602	482	572	439	588
Test-5	363	450	358	463	494	594	447	578	486	569	365	488
Test-6	347	452	336	446	449	565	434	542	491	568	366	488
Avg	357	460	337	451	464	573	460	579	448	548	383	520

Table 3. Fracture deformation and percentage elongation (unit: deformation in mm).

	Base metal				Weld				HAZ			
	Longitudinal		Transverse		Longitudinal		Transverse		Longitudinal		Transverse	
	D_f	δ_f	D_f	δ_f	D_f	δ_f	D_f	δ_f	D_f	δ_f	D_f	δ_f
Test-1	2.88	0.32	1.14	0.57	2.34	0.26	0.58	0.29	1.63	0.18	0.78	0.39
Test-2	2.20	0.24	1.27	0.64	2.46	0.27	0.87	0.44	2.26	0.25	0.71	0.36
Test-3	2.84	0.32	1.30	0.65	1.53	0.17	1.01	0.51	2.10	0.23	0.78	0.39
Test-4	2.16	0.24	0.88	0.44	2.04	0.23	1.01	0.51	1.41	0.16	0.92	0.46
Test-5	3.06	0.34	1.16	0.58	2.24	0.25	0.72	0.36	1.71	0.19	0.67	0.34
Test-6	2.48	0.28	1.23	0.62	2.56	0.28	0.78	0.39	1.85	0.21	0.63	0.32
Avg	2.60	0.29	1.16	0.58	2.19	0.24	0.83	0.42	1.83	0.20	0.75	0.38

3.2 HARDNESS-STRENGTH RELATIONSHIP

As mentioned in the introduction, one of the methods to obtain the yield and tensile strengths of the weld and HAZ is to use empirical hardness-strength correlation functions. Pavlina et al. [10] investigated the correlations for over 150 steel grades covering different compositions and microstructures, and proposed the following equations through regression analysis:

$$\sigma_y = -90.7 + 2.876Hv \tag{1}$$

$$\sigma_u = -99.8 + 3.734Hv \tag{2}$$

where the yield and ultimate tensile strengths are in MPa.

In order to verify the precision of the equations in predicting the material strengths of the weld and HAZ, Fig. 12 compares the equations to the measurements of this study. In Section 2.2, the surfaces on which the hardnesses were measured were perpendicular to the longitudinal direction, and, hence, the measured hardnesses were related to the material strengths in the longitudinal direction. The ±10% boundaries of Eqs. (1) and (2) are also shown in Fig. 12, plotted using dotted lines.

It is observed that while the equations can provide reasonably good predictions for the base metal and HAZ, they tend to overestimate the strength of the weld.

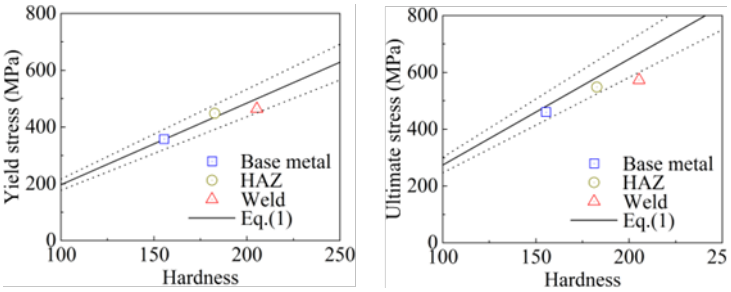

(a) Yield strength (b) Tensile strength

Fig. 12. Relationship between yield and ultimate strengths versus hardness.

3.3 TRUE STRESS-STRAIN RELATIONSHIPS

Prior to the commencement of necking, the true stress and strain (i.e., σ_{true} and ε_{true}) were calculated from the engineering stress and strain (i.e., σ_{eng} and ε_{eng}) using the following equations:

$$\varepsilon_{true} = \ln(1 + \varepsilon_{eng}) , \tag{3}$$

$$\sigma_{true} = \sigma_{nom} \left(1 + \varepsilon_{eng}\right) . \tag{4}$$

According to [29], the post-necking true stress-strain relationship was assumed to be linear, and the post-necking strain hardening modulus could be determined by trial-and-error finite element analyses. Thus, the true stress-strain curves were calculated for all miniature flat plate coupons, and the true stress-strain curve of each material in each direction was obtained, as plotted in Fig. 13, by averaging the curves of corresponding coupon tests.

The miniature flat plate tests were numerically reproduced using the commercial FE software ABAQUS. The materials were modelled by isotropic von Mises plasticity with the true stress-strain curves shown in Fig. 13. Eight-node linear solid elements with reduced integration (C3D8R) were used with the element size being 0.2 mm in the parallel part. The load-deformation curves obtained from the FE simulations agreed well with the test curves, as shown in Figs. 10 and 11. Note that in the FE models, fracture propagation was not simulated, and therefore, the FE curves did not drop due to the onset of fracture but continued to develop deformation. The point corresponding to the average fracture deformation listed in Table 3 was plotted on each FE curve.

The tests of the FPL-standard coupons were also modelled in ABAQUS, with the true stress-strain relationship obtained from the miniature FPLs of the base metal, i.e., the solid black line in Fig. 13(a). Fig. 14 compares the FE and test curves, which show a good agreement, confirming again that the tests of miniature coupons and conventional size coupons gave consistent results.

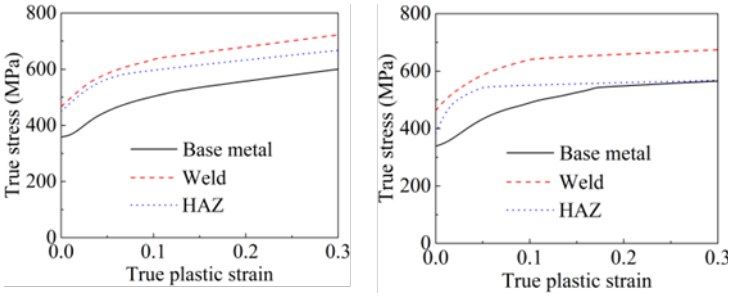

(a) Longitudinal (b) Transverse

Fig. 13. Stress-strain curves.

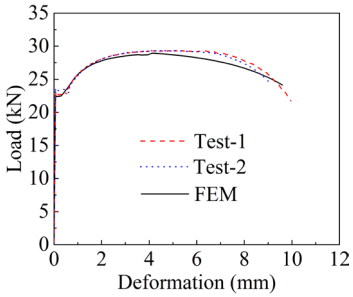

Fig. 14. Load-deformation curves of FPL-standard coupons.

4 FRACTURE STRAINS AT DIFFERENT STRESS STATES

4.1 TEST RESULTS OF NOTCHED ROUND BARS AND GROOVED PLATES

Fig. 15 shows tests of the miniature NRB and GP coupons. During the loading process, plastic deformation localized in the notched parts where the final fracture occurred. The load-deformation curves for the NRB coupons extracted in longitudinal (i.e., NRB-L) and transverse directions (i.e., NRB-T) are plotted in Figs. 16-17, respectively, and the curves for the GP coupons extracted in longitudinal (i.e., GP-L) and transverse directions (i.e., GP-T) are plotted in Figs. 18-19, respectively. The deformations corresponding to the onset of fracture, after which the load dropped instantly, are summarised in Table 4.

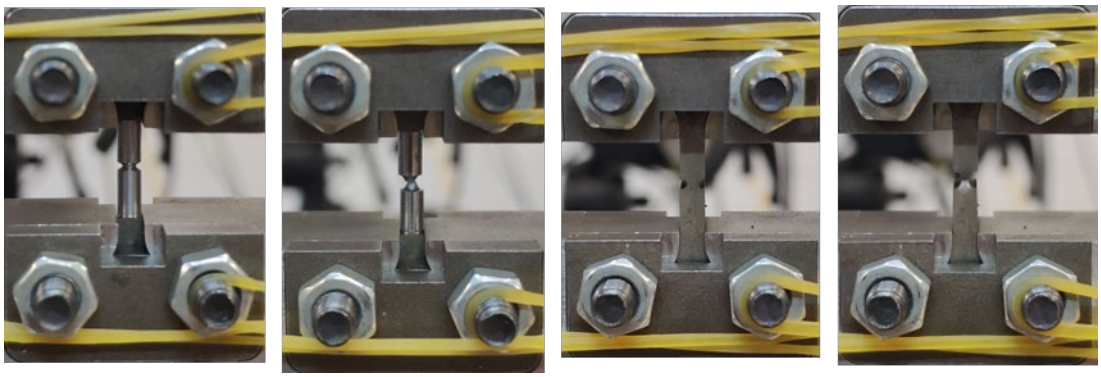

Before loading Fractured Before loading Fractured

(a) NRB (b) GP

Fig. 15. Miniature notched round bars and grooved plates for base metal.

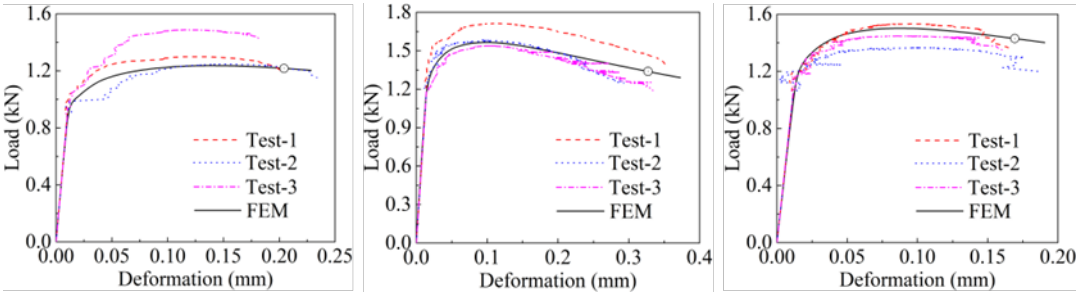

(a) Base metal (b) Weld (c) HAZ

Fig. 16. Load-deformation curves of NRB-L coupons.

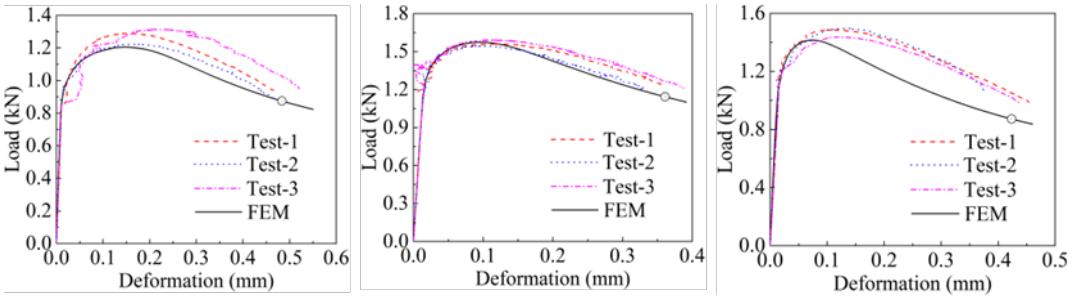

(a) Base metal (b) Weld (c) HAZ

Fig. 17. Load-deformation curves of NRB-T coupons.

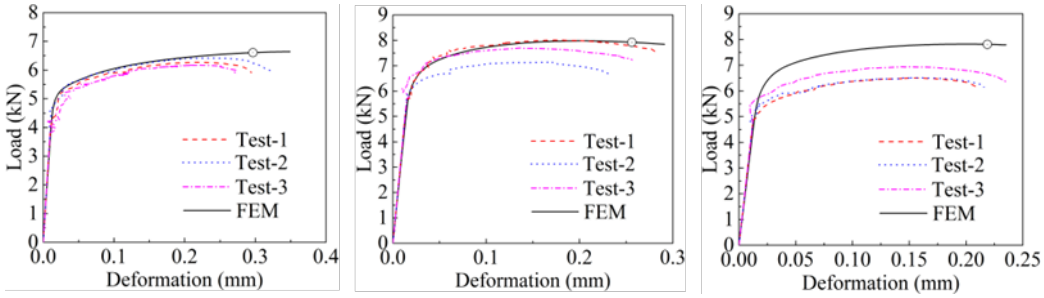

(a) Base metal (b) Weld (c) HAZ

Fig. 18. Load-deformation curves of GP-L coupons.

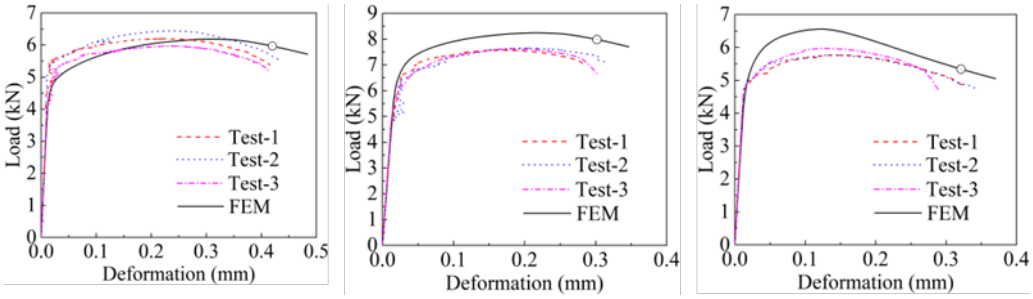

(a) Base metal (b) Weld (c) HAZ

Fig. 19. Load-deformation curves of GP-T coupons.

Table 4. Fracture deformations (D_f) of NRBs and GPs (mm).

	NRB						GP					
	Longitudinal			Transverse			Longitudinal			Transverse		
	BM	Weld	HAZ	BM	Weld	HAZ	BM	Weld	HAZ	BM	Weld	HAZ
Test-1	0.20	0.36	0.16	0.47	0.36	0.46	0.29	0.28	0.21	0.42	0.28	0.33
Test-2	0.23	0.29	0.19	0.47	0.33	0.38	0.32	0.23	0.22	0.44	0.31	0.34
Test-3	0.18	0.33	0.16	0.52	0.39	0.44	0.28	0.26	0.23	0.41	0.30	0.29
Avg	0.20	0.33	0.17	0.49	0.36	0.43	0.30	0.26	0.22	0.42	0.30	0.32

4.2 FRACTURE STRAINS

The tests of the miniature NRB and GP coupons were simulated in ABAQUS using the same modelling strategy as in Section 3.2. The measured dimensions of the coupons were used, and the true stress-strain relationships obtained from the miniature FPL and FPT coupons (i.e., Fig. 13) were adopted.

Figs. 16-19 compare the FE simulated load-deformation curves with the experimental curves. Without defining a fracture model (which shall be validated in Section 5) in the FE models, the FE curves did not detect the onset of fracture and continued to develop large deformations under a gradually decreasing load. The points corresponding to the fracture deformations in Table 4 are plotted on the FE curves. A good agreement between the experimental and FE curves is observed prior to the fracture points.

Together with the miniature FPs, these miniature coupons represented different stress states, which can be characterised by the stress triaxiality, T, and Lode angle parameter, ξ. The two parameters are functions of the normalised first invariant of the stress tensor, I_1, and the normalised third invariant of the stress deviator tensor, J_3, respectively:

$$T = \frac{I_1}{3\bar{\sigma}} \tag{5}$$

$$\xi = \frac{27 J_3}{2\bar{\sigma}^3}, \tag{6}$$

where $\bar{\sigma}$ is the von Mises stress. ξ relates to the Lode angle, θ, through:

$$\xi = \cos(3\theta). \tag{7}$$

Since the range of θ is between 0 and $\pi/3$, ξ ranges between -1 and 1. Considering the values of T and ξ normally do not stay constant during plastic loading, their average values over the loading history should be used as the representative values, which are calculated as:

$$T_{avg} = \frac{1}{\varepsilon_f}\int_0^{\varepsilon_f} T d\varepsilon_p \tag{8}$$

$$\xi_{avg} = \frac{1}{\varepsilon_f}\int_0^{\varepsilon_f} \xi d\varepsilon_p, \tag{9}$$

where ε_f and ε_p are the fracture strain and equivalent plastic strain, respectively. For each coupon type, the value of ε_f was obtained from the FE models as the value of ε_p at the centre of the cross-section where plastic strains localised and fracture initiated, at the deformation (D_f) corresponding to the fracture deformations shown in Tables 3 and 4. Similarly, the values of T_{avg} and ξ_{avg} represented by each coupon type were computed by integrating the values of T and ξ calculated from the stress and strain tensors obtained from the FE models.

Table 5 summarises the values of ε_f, T_{avg} and ξ_{avg}. The FP and NRB coupons exhibited stress states with ξ_{avg}-values of approximately 1, low T_{avg}-values ranging from 0.40 to 0.59 and high T_{avg}-values ranging from 1.04 to 1.25. The GP coupons had high T_{avg}-values of about 1.15 and ξ_{avg} varying from 0.04 to 0.47. The GP coupons were intended to produce a plane strain stress state, for which the value of ξ is zero, but for certain coupons, ξ_{avg}-values significantly larger than zero occurred because the measured widths of the notched part were larger than the nominal values (e.g., 1.2 mm vs. 1.0 mm) due to imprecise machining of the miniature coupons. In Fig. 20, the values of ε_f for the BM, weld and HAZ in the longitudinal and transverse directions are plotted against T and ξ. The following observations are made from the test results:

(1) The fracture strains of the BM and HAZ were generally larger in the transverse direction than in the longitudinal direction, with the ratio of fracture strains in the two directions (averaged between FP, NRB and GP coupons) being 2.56 and 2.71 for the BM and HAZ, respectively. This demonstrated the anisotropy of the fracture-related properties of the BM and HAZ.

(2) By contrast, the weld is nearly isotropic in terms of fracture strain, with the ratio of fracture strains in the two directions (averaged between FP, NRB and GP coupons) being 0.99. The isotropic characteristic of the weld can also be demonstrated by the similar values of yield stress, tensile strength, fracture deformation and percentage elongation in the two directions, as shown in Tables 2 and 3. This is not surprising as the fusion zone was not subjected to the same rolling effects as the BM, which also affected the properties of the HAZ.

(3) The HAZ and base metal had similar fracture strains in both the longitudinal and transverse directions. The weld showed larger fracture strains than those of the HAZ and base metal in the longitudinal direction, but smaller fracture strains in the transverse direction.

Table 5. Stress states and fracture strains of miniature coupons.

		FP			NRB			GP		
		T_{avg}	ξ_{avg}	ε_f	T_{avg}	ξ_{avg}	ε_f	T_{avg}	ξ_{avg}	ε_f
Longitudinal	Base metal	0.40	0.97	0.82	1.04	1.00	0.18	1.08	0.47	0.10
	Weld	0.44	0.93	0.94	1.13	1.00	0.42	1.18	0.16	0.18
	HAZ	0.44	0.94	0.80	1.14	1.00	0.18	1.16	0.27	0.11
Transverse	Base metal	0.49	0.89	0.90	1.08	1.00	0.61	1.10	0.18	0.32
	Weld	0.49	0.91	0.69	1.20	1.00	0.50	1.18	0.18	0.19
	HAZ	0.59	0.77	0.78	1.25	1.00	0.62	1.20	0.04	0.41

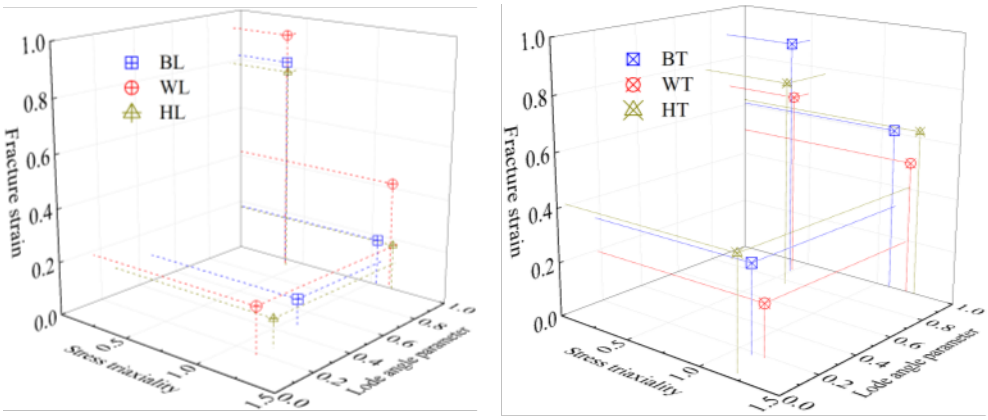

(a) Longitudinal (b) Transverse

Fig. 20. Stress states and fracture strains of base metal, weld and HAZ.

5 FRACTURE MODELS OF BASE METAL, WELD AND HAZ

A new fracture model termed the Lode angle modified void growth model (LMVGM) was proposed in [19] based on comprehensive experimental data. In LMVGM, the effects of stress triaxiality and Lode angle parameter are described using the void growth-based exponential function and an additional exponential term, respectively. Fracture is expected to initiate when the damage index D,

$$D = \int_{\varepsilon_p} \frac{1}{\alpha} \cdot e^{\beta \cdot T - \gamma \cdot \xi} d\varepsilon_p \tag{10}$$

reaches unity where α, β and γ are free parameters. Alternatively, the average values of T and ξ can be used to accommodate the variations in T and ξ during the loading history, simplifying Eq. (10) to:

$$\varepsilon_f = \alpha \cdot e^{-\beta \cdot T_{avg} + \gamma \cdot \xi_{avg}}. \tag{11}$$

Using Eq. (11), the fracture parameters α, β and γ were calculated based on the experimental data listed in Table 5, as summarised in Table 6. Based on the calibrated LMVGM model, the fracture surfaces in the space of stress triaxiality, Lode angle parameter and fracture strain are

plotted in Figs. 21 and 22, where the marked points represent test data. Comparing the fracture surfaces of different materials, Fig. 23 shows the material with the lowest fracture strain at any given combination of stress triaxiality and Lode angle parameter. The following observations are made:

(1) All fracture surfaces tilt towards stress states with high T and low ξ values, i.e., ε_f increased with a decrease in T and an increase in ξ, indicating that fracture can initiate more easily when the materials are subjected to high T and low ξ values.

(2) For all three materials, the longitudinal fracture strains were higher than their transverse counterparts at low stress triaxialities but decreased at a steeper slope with increasing stress triaxiality, eventually becoming lower than the transverse fracture strains at high stress triaxialities.

(3) In the longitudinal direction, the base metal and weld had the lowest fracture strains at high and low stress triaxiality, respectively; the boundary was around T = 0.3 depending on the Lode angle parameter. In the transverse direction, the weld had the lowest fracture strain for all stress states. HAZ never showed the smallest fracture strain, which, at first glance, seemed contradictory to the data presented in Table 5, in which the HAZ had the smallest fracture strain for longitudinal FP. However, the fracture strains in Table 5 correspond to slightly different stress states.

Table 6. Fracture parameters of LMVGM.

		α	β	γ
Longitudinal	BM	0.97	2.44	0.84
	Weld	0.72	1.27	0.89
	HAZ	1.21	2.23	0.62
Transverse	BM	0.67	0.79	0.75
	Weld	0.32	0.62	1.17
	HAZ	0.73	0.51	0.47

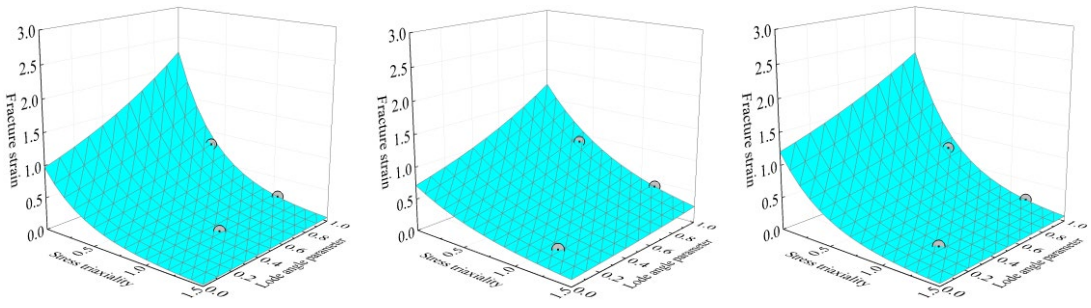

(a) Base metal (b) Weld (c) HAZ

Fig. 21. Predicted fracture loci in the longitudinal direction.

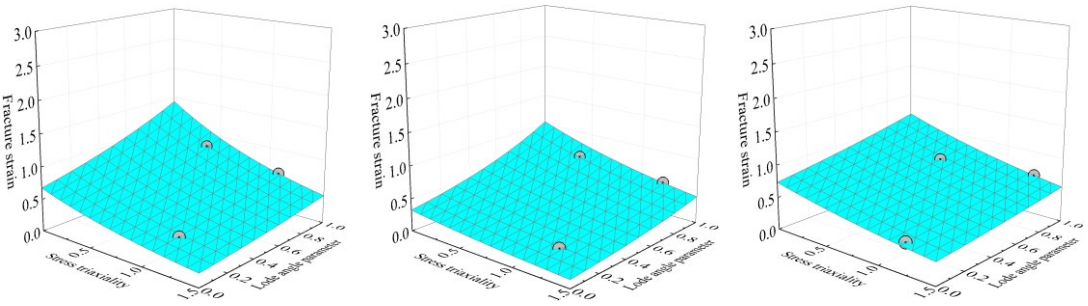

(a) Base metal (b) Weld (c) HAZ

Fig. 22. Predicted fracture loci in the transverse direction.

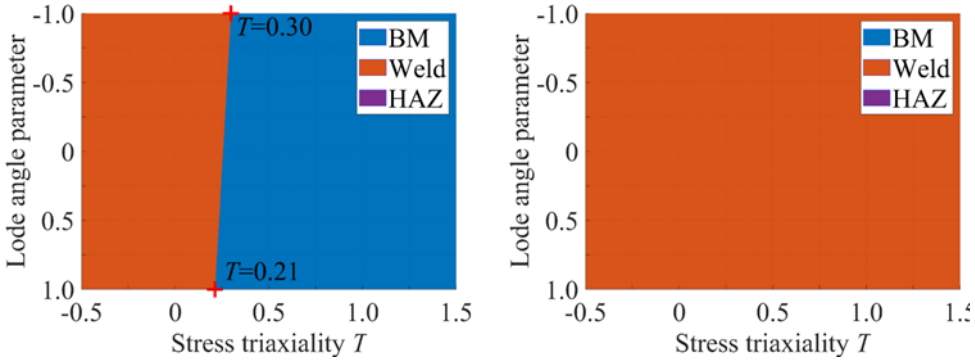

(a) Longitudinal (b) Transverse

Fig. 23. Material with the lowest fracture strain.

6 CONCLUSIONS

This paper determines the strengths and fracture strains of the weld and HAZ materials in both the longitudinal and transverse directions of the weld, and compares the values to those of the base metal. The major conclusions are summarised as follows:

(1) Stress-strain relationship. The base metal showed similar and repeatable stress-strain relationships in the longitudinal and transverse directions, while the weld and HAZ were relatively less homogeneous and showed large variations in terms of both the onset of yielding and post-yielding response.

(2) Yield and tensile strength. In both directions, the yield and tensile strengths of the HAZ were higher than those of the base metal but lower than those of the weld. For base metal and HAZ, the yield and tensile strengths in the longitudinal direction were higher than their transverse counterparts, while the strengths of the weld were nearly independent of direction.

(3) The hardness-strength relationship. The yield and tensile strengths of the weld and HAZ can be approximated using the empirical hardness-strength correlation functions proposed by Pavlina et al. [10], except that the functions tend to overestimate the strengths of the weld by about 10%.

(4) Fracture strain. The HAZ had similar fracture strains to the base metal in both the longitudinal and transverse directions, and their fracture strains were generally larger in the transverse direction than in the longitudinal direction, demonstrating the anisotropy of the fracture-related properties of

the BM and HAZ. By contrast, the weld was generally isotropic in terms of fracture strain. For the stress states represented by the tests, the weld showed larger fracture strains than those of the HAZ and base metal in the longitudinal direction, but smaller fracture strains in the transverse direction.

(5) Fracture models and fracture surfaces. The fracture model LMVGM can be used to predict the fracture strains of weld and HAZ at a given stress state. The model parameters were calibrated and shown in Table 6. All fracture surfaces tilted towards stress states with high stress triaxiality and low Lode angle parameter, indicating that fracture can initiate more easily at these stress states. In the longitudinal direction, the base metal and weld had the lowest ductility at high and low stress triaxialities, respectively; the boundary was between T = 0.21 to 0.30, depending on the Lode angle parameter. In the transverse direction, the weld had the lowest ductility for all stress states. HAZ never showed the lowest ductility.

Note that the conclusions of this paper are limited to the tested AS350 grade steel and accompanying weld, laid using grade B-G49 welding wire.

7 ACKNOWLEDGEMENTS

This work was supported by the Australian Research Council through Discovery Project [grant number DP190103737]; the National Natural Science Foundation of China [grant number 52178152]; and an AINSE Ltd. Postgraduate Research Award (PGRA).

References

[1] Pham, T.H. and Kim, S.E., 2015. Determination of mechanical properties in SM490 steel weld zone using nanoindentation and FE analysis. *Journal of Constructional Steel Research*, *114*, pp.314-324.

[2] Ma, Y., Takikawa, A., Nakanishi, J., Doira, K., Shimizu, T., Lu, Y. and Ma, N., 2021. Measurement of local material properties and failure analysis of resistance spot welds of advanced high-strength steel sheets. *Materials & Design*, *201*, p.109505.

[3] Song, Q.Y., Heidarpour, A., Zhao, X.L. and Han, L.H., 2018. Experimental and numerical investigation of ductile fracture of carbon steel structural components. *Journal of Constructional Steel Research*, *145*, pp.425-437.

[4] Yelek, İ., Ardalı, R. and Yılmaz, İ., 2021. Fracture investigation of different welded steel beam-column connections under three-point bending test. *Journal of Constructional Steel Research*, *187*, p.106945.

[5] Wang, Y., Zhou, H., Shi, Y. and Xiong, J., 2011. Fracture prediction of welded steel connections using traditional fracture mechanics and calibrated micromechanics based models. *International Journal of Steel Structures*, *11*, pp.351-366.

[6] Zhu, C., Rasmussen, K.J.R., Yan, S. and Zhang, H., 2019. Experimental full-range behavior assessment of bolted moment end-plate connections. American Society of Civil Engineers.

[7] Zerbst, U., Ainsworth, R.A., Beier, H.T., Pisarski, H., Zhang, Z.L., Nikbin, K., Nitschke-Pagel, T., Münstermann, S., Kucharczyk, P. and Klingbeil, D., 2014. Review on fracture and crack propagation in weldments–A fracture mechanics perspective. *Engineering fracture mechanics*, *132*, pp.200-276.

[8] Khalfallah, A., 2014. Experimental and numerical assessment of mechanical properties of welded tubes for hydroforming. *Materials & Design (1980-2015)*, *56*, pp.782-790.

[9] Peng, Y., Wu, C., Gan, J. and Dong, J., 2019. Characterization of heterogeneous constitutive relationship of the welded joint based on the stress-hardness relationship using micro-hardness tests. *Construction and Building Materials*, *202*, pp.37-45.

[10] Pavlina, E.J. and Van Tyne, C.J., 2008. Correlation of yield strength and tensile strength with hardness for steels. *Journal of materials engineering and performance*, *17*, pp.888-893.

[11] Wudtke, I., Talebi, H., Silani, M. and Werner, F., 2015. A hierarchical multi-scale approach to mechanical characterization of heat affected zone in welded connections. *Computational Materials Science*, *96*, pp.396-402.

[12] Yang, B., Xuan, F.Z. and Chen, J.K., 2018. Evaluation of the microstructure related strength of CrMoV weldment by using the in-situ tensile test of miniature specimen. *Materials Science and Engineering: A*, *736*, pp.193-201.

[13] Hval, M., Thaulow, C., Lange, J.H., Hoydal, S.H. and Zhang, Z.L., 1998. Numerical modeling of ductile fracture behavior in aluminum weldments. *WELDING JOURNAL-NEW YORK-*, *77*, pp.208-s.

[14] Wei, C., Zhang, J., Yang, S., Tao, W., Wu, F. and Xia, W., 2015. Experiment-based regional characterization of HAZ mechanical properties for laser welding. *The International Journal of Advanced Manufacturing Technology*, *78*, pp.1629-1640.

[15] Peng, Y., Wu, C., Gan, J. and Dong, J., 2018. Determination of the local constitutive properties of the welded steel joints using digital image correlation method. *Construction and Building Materials*, *171*, pp.485-492.

[16] Ran, M.M., Sun, F.F., Li, G.Q., Kanvinde, A., Wang, Y.B. and Xiao, R.Y., 2019. Experimental study on the behavior of mismatched butt welded joints of high strength steel. *Journal of Constructional Steel Research*, *153*, pp.196-208.

[17] Wierzbicki, T., Bao, Y. and Bai, Y., 2005, June. A new experimental technique for constructing a fracture envelope of metals under multi-axial loading. In *Proceedings of the 2005 SEM annual conference and exposition on experimental and applied mechanics* (Vol. 1, pp. 1295-1303). Portland USA.

[18] Smith, C.M., Deierlein, G.G. and Kanvinde, A.M., 2014. A stress-weighted damage model for ductile fracture initiation in structural steel under cyclic loading and generalized stress states. *Technical Rep*, *187*.

[19] Liu, X., Yan, S., Rasmussen, K.J. and Deierlein, G.G., 2022. Experimental investigation of the effect of Lode angle on fracture initiation of steels. *Engineering Fracture Mechanics*, *271*, p.108637.

[20] Kanvinde, A.M., Fell, B.V., Gomez, I.R. and Roberts, M., 2008. Predicting fracture in structural fillet welds using traditional and micromechanical fracture models. *Engineering Structures*, *30*(11), pp.3325-3335.

[21] Liao, F., Wang, W. and Chen, Y., 2012. Parameter calibrations and application of micromechanical fracture models of structural steels. *Structural Engineering and Mechanics*, *42*(2), pp.153-174.

[22] Mae, H., Teng, X., Bai, Y. and Wierzbicki, T., 2007. Calibration of ductile fracture properties of a cast aluminum alloy. *Materials Science and Engineering: A*, *459*(1-2), pp.156-166.

[23] Gorji, M.B. and Mohr, D., 2017. Micro-tension and micro-shear experiments to characterize stress-state dependent ductile fracture. *Acta Materialia*, *131*, pp.65-76.

[24] Pandya, K.S., Grolleau, V., Roth, C.C. and Mohr, D., 2020. Fracture response of resistance spot welded dual phase steel sheets: Experiments and modeling. *International Journal of Mechanical Sciences*, *187*, p.105869.

[25] AS/NZS 3678. Structural Steel–Hot-rolled plates, floor plates and slabs. Standards Australia, Sydney, 2011.

[26] AS/NZS 1554. Structural steel welding. Standards Australia, Sydney, 2014.

[27] AS 1391. Metallic Materials – Tensile Testing at Ambient Temperature. Standards Australia, Sydney; 2020.

[28] Huang, Y. and Young, B., 2014. The art of coupon tests. *Journal of Constructional Steel Research*, *96*, pp.159-175.

[29] Yan, S., Jiang, L., Rasmussen, K.J.R. and Zhang, H., 2021. Full-range behavior of top-and-seat angle connections. *Journal of Structural Engineering*, *147*(1), p.04020308.